Supplementary Material for The Development and Benchmarking of JANGOFETT: A Geant4-Based Fission Event Tracking Tool

Liam Walker[1], Jack Shire[1], Jacob Jaffe[1], Payton Sprando[1], Jack Olinger[1], and Alexander Chemey[1]

[1]Department of Nuclear Science and Engineering, Oregon State University, Corvallis, OR 97331, United States

1 Simulation Geometry

The design of the detector system used for analysis of JANGOFETT is illustrated in Fig S.1. A custom scattering chamber was centered in the simulation world, constructed of aluminum with a 50 μm thick sphere of polyethylene terephthalate (Mylar). Two 100 cm^2 silicon detectors of 300 micron thickness used for charged particle spectroscopy. These were placed on opposite sides at an offset of 4 cm from the center of the detector to the source. At the center of the chamber primary fission products (PFPs) were emitted from the origin.

The detector system simulated in Geant4(Agostinelli et al.) included 21 high-purity germanium (HPGe) detectors arranged equidistantly around the PFP source location were at a distance of ∼20 cm. Detectors were placed orthogonal to each face of a truncated cuboctahedron scattering chamber comprised of 8 triangular surfaces and 18 square surfaces. Two square face detectors openings were removed for simulated up- and downstream beam port locations, and 3 square faces in the lower hemisphere were removed due to constraints with the real-world floor (not modeled).

Each HPGe was surrounded by an annular bismuth germanium oxide (BGO) active veto detector for Compton suppression. Simulated HPGe detector geometries included genericized planar, coaxial, and clover-style detectors, ranging from ∼15% to ∼80% relative efficiency. Clover detectors included add-back routines that emulate larger single crystal efficiencies. All detectors were simulated with aluminum housings surrounding the whole crystal, with the exception of planar detectors, where the face near the scattering chamber was replaced with a thin beryllium window to allow for low energy photon transmission. Crystals had attached back-mounted structures representing structural components to improve simulation of scattering. Coincidence logic was used to veto photons detected in the HPGe and in the corresponding BGO shield within a 10 ns timing window .

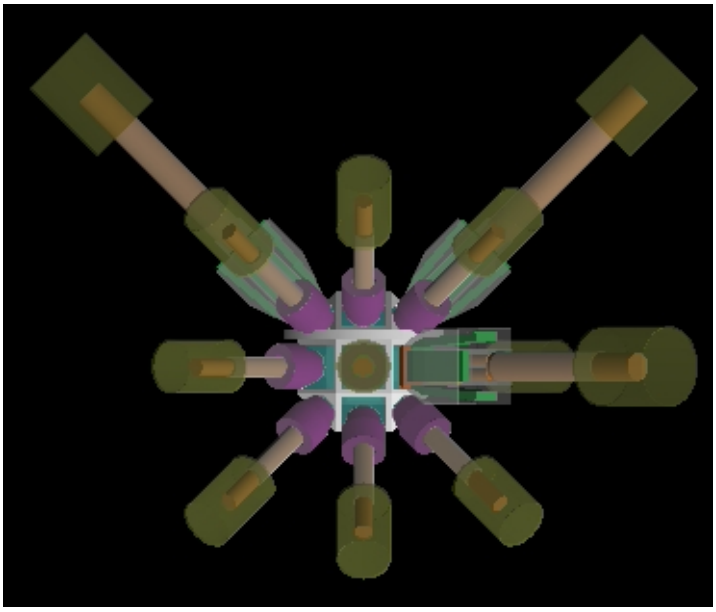


Figure S.1: Ray traced render of the Geant4 world geometry. All detectors were placed such that the detector faces were ∼20 cm from the origin. Color code: Teal is the scattering chamber Mylar window, silver is the Aluminum scattering chamber structure and aluminum detector housing, light green are BGO crystals for the clover detectors, purple are BGO detector housings for the planar and coaxial detectors, brown is a copper "cold finger" standard component, and off-yellow is the dewar for the detectors. HPGe crystals and silicon detectors are not visible in this image as they are internal to other components.

2 Coincidence Timing

The identification of the γ-coincidence timing window was performed by analyzing the timing between PFPs and coincident prompt γ pulses in Fig S.2. First, the average time between coincident PFP triggers in the silicon detectors was determined to be less than 5 ns. Then, a secondary timing window was defined around this average to effectively capture the majority of coincident prompt γ-rays, as illustrated in Fig. S.2. A broad coincidence window of -30 ns to 20 ns was selected for silicon-HPGe coincidences, where t = 0 is chosen to be the average silicon detector trigger time for valid silicon-silicon coincidence events with deposited energy greater than 20 MeV. With this timing established, the coincidence information was extracted as correlated events, enabling straightforward filtering between light and heavy fragment pairs, as well as PFP-γ coincidences.

3 Total Kinetic Energy

Total kinetic energy was calculated by summing the energy depositions within the silicon detectors that occurred within 20 ns of each other. Due to the nature of beam-line experiments, there is a chance that 3 or 4 fragments may hit the detectors in this time, creating a false coincidence. It was important that this simulation be able to demonstrate the ability to reproduce this effect to replicate the noise expected in real life experiments. This is shown clearly in Fig S.3, where the false coincidences extend from 230 to 400 MeV of "TKE", although CGMF input TKE never exceeded 225 MeV. Note that the 4-

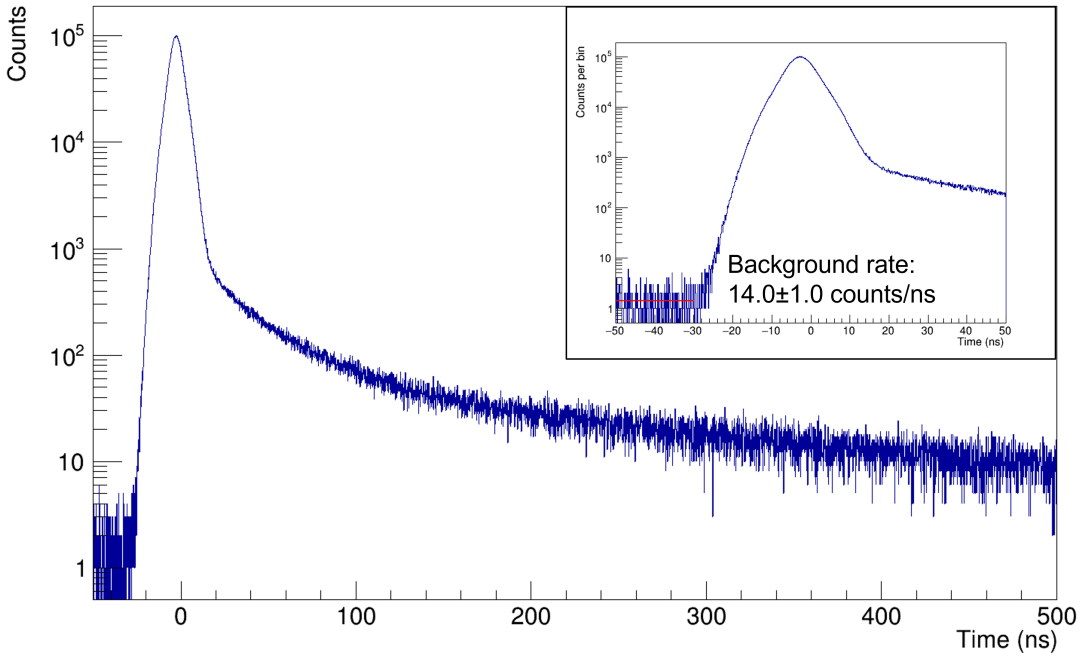


Figure S.2: Coincidences for γ pulses near the averaged time for a coincident pair of PFP pulses from -50 ns to +500 ns vs the average silicon detector trigger time. The trigger window was set to -30 ns to +20 ns for all analysis in this work. The main peak is centered at -2.85 ns. This agrees with estimations based on time of flight for PFPs vs photons interacting within the HPGe detectors. The region before the peak from -50 to -30 ns was averaged to yield a random event rate of 14.0 $\pm$ 1.0 counts per ns with 87 million fissions. The inset displays a smaller region of (-50, 50) ns for clarity.

fragment cluster is larger than the 3-fragment cluster. This is due to the geometry of the simulation - PFP are emitted at almost 180° in the lab frame, with small deviations for momentum transfer from emitted neutrons, so if one fragment is detected, its complement is also likely to be detected. These multi-hit events occurred a total of 793 times of the 7.12×10^7 fission fragment silicon detector pulses recorded, 0.0011% of the time. Given a timing coincidence window of 20 ns, a solid angle of 40% of 2π, and a mean time between fissions of 1 ms, this is within 50% of the calculated rate. Future simulations will require a target to properly account for kinetic energy losses, as one was not simulated here. Furthermore, all fragments were emitted as neutral charged particles, which prevented X-rays from being emitted. Version 1.0 is presented without a target. Version 1.01 has been released in the proofing stage and incorporates both targets and half-filled electron shells for X-ray generation in targeted detectors.

A potential source of error would be a systematic bias in Geant4 or our analysis code, one that did not match the inputs from CGMF. This is most easily checked by comparing TKE values from CGMF and the output from Geant4, both in mean TKE and in the distribution of TKE. Shown in Fig S.4 are the mean TKE for Geant4 outputs and CGMF inputs. These data are in reasonable agreement. The distribution from Geant4 is slightly flatter than the inputs, which is to be expected given the blurring applied to the detectors, and is shifted very modestly (4$\pm$4 keV) to the low-energy side, due to secondary particles and X-rays emitted from the surface of the silicon detectors. Standard deviations of the

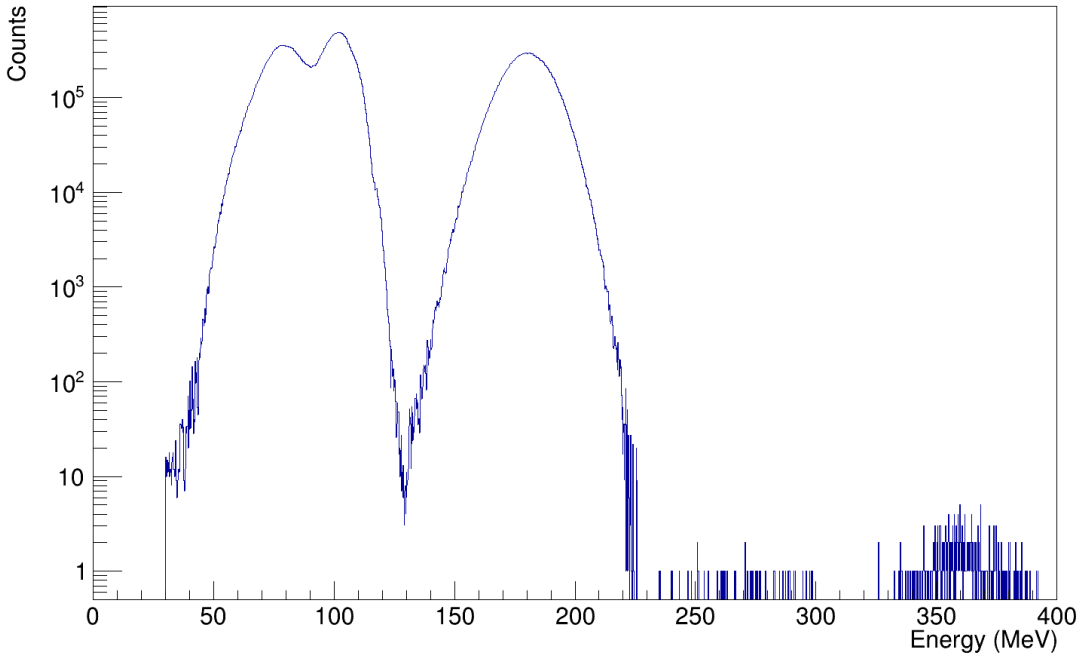


Figure S.3: Charged particle spectra from DSSD pulses. Shown here is the TKE and KE on the same figure (see text for fit information). Note that there are a small number of events beyond the edge of the actual coincident TKE events (beyond 230 MeV) representing false coincidences. The first small cluster from about 230-300 MeV are the 3 fragment coincidences, and the 320-400 MeV cluster is the double pair (4 fragment) coincidences.

fit (σ) are consistent as well, only differing as the Geant4-simulated distribution is 4.5 keV broader due to the Gaussian blurring.

4 Additional Gated Fragments

In addition to ^{144}Ba, ^{141}Cs, ^{149}Nd, and ^{150}Ce were also gated on using the methods described in section 3.3 of the paper. All of the γ-γ-γ histograms for the respective fragments are provided below, as are the γ gates, selected from the Brookhaven NNDC data for excited states of each isotope, utilizing NuDat3 data (National Nuclear Data Center, 2025).

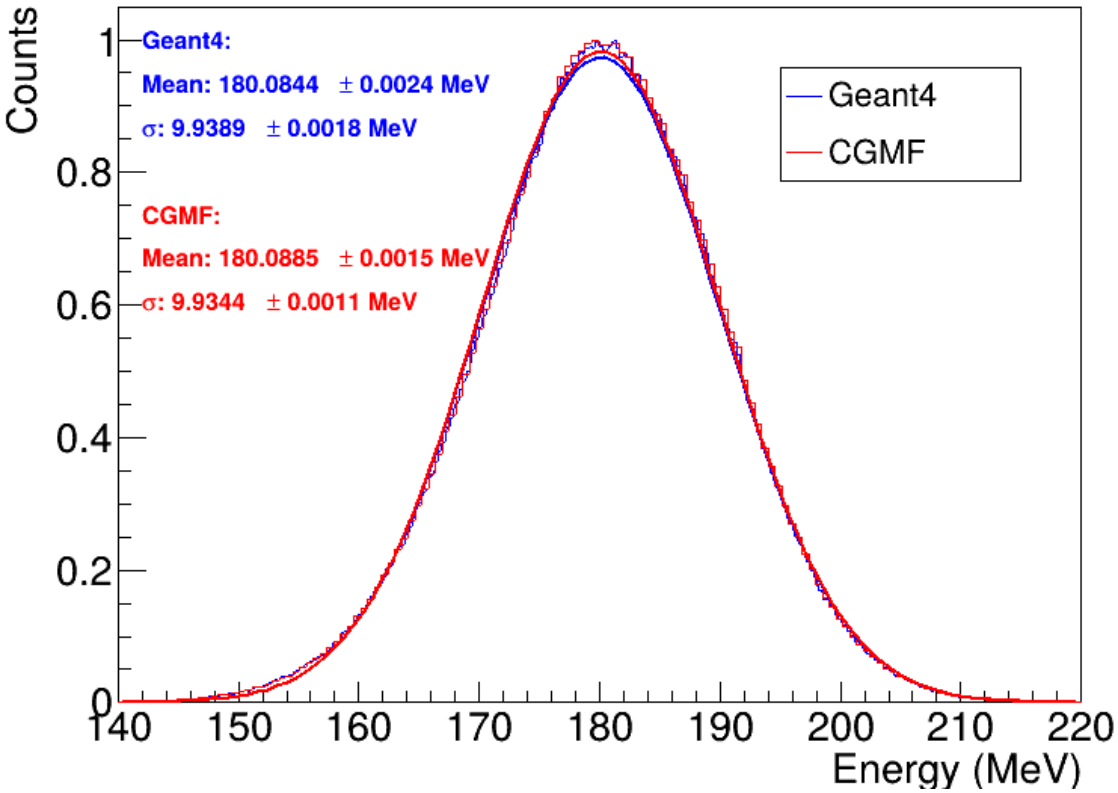
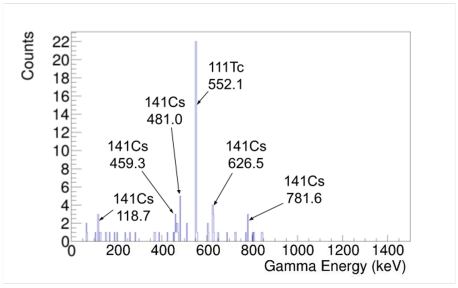
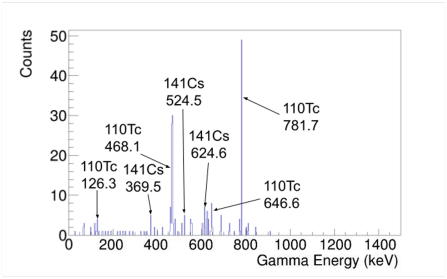


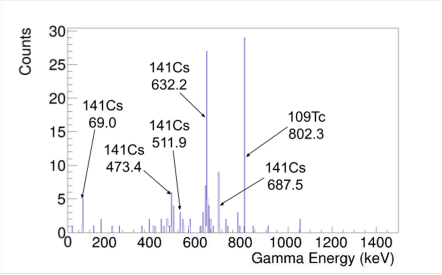
Figure S.4: Overlayed and normalized TKE for the simulated data, with Gaussian fits, before and after CGMF inputs are simulated in Geant4. Geant4 outputs are consistent with CGMF inputs.



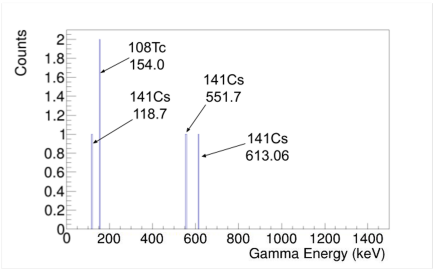
(a) 0n



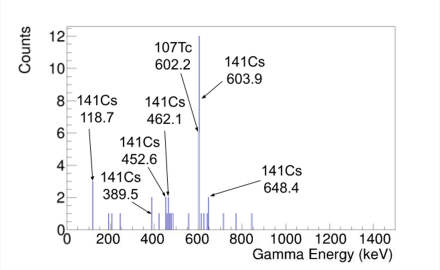
(b) 1n



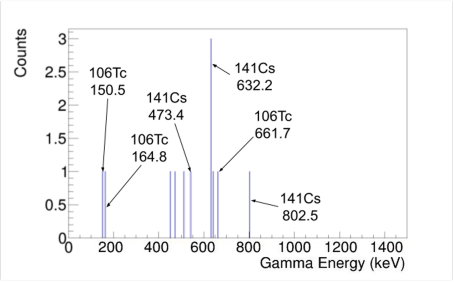
(c) 2n



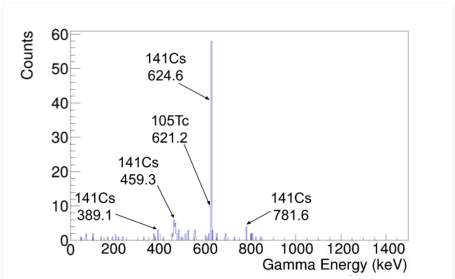
(d) 3n



(e) 4n

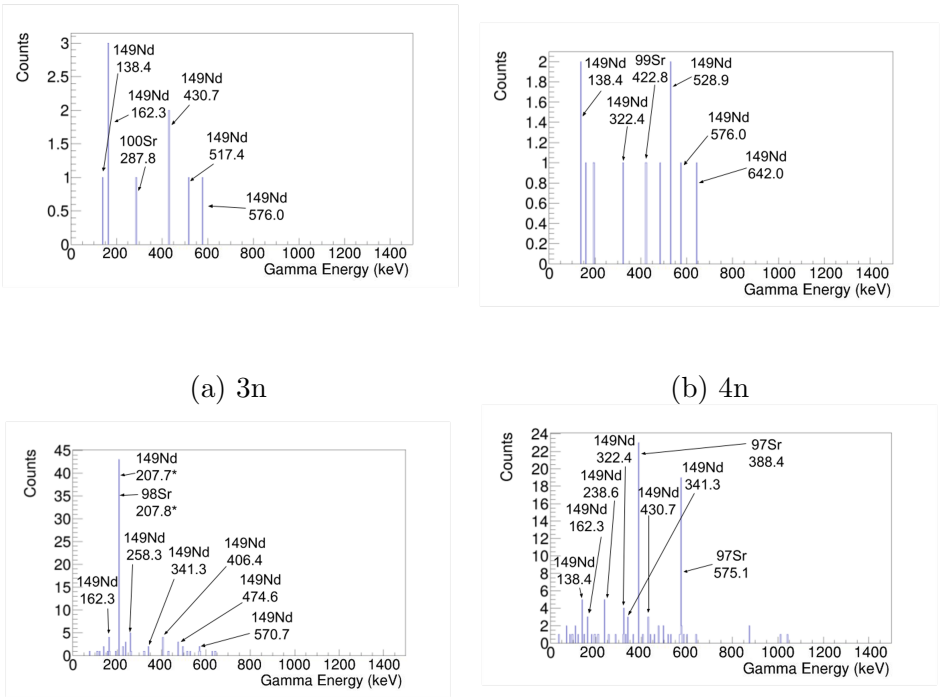


(f) 5n



(g) 6n

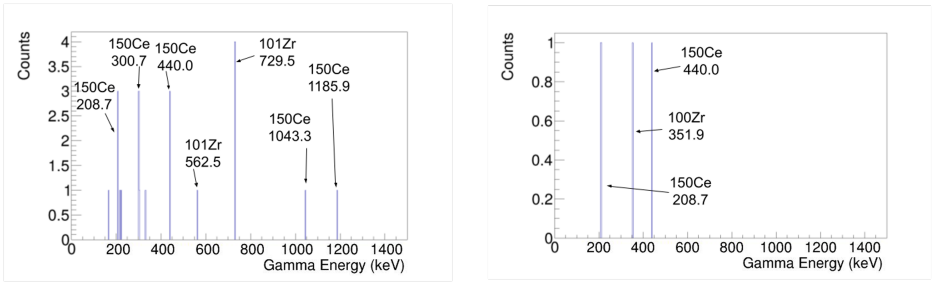
Figure S.5: γ energy spectra when at least two coincident γ from ^{141}Cs and at least one γ from the correlated light fragment (i.e. $^{252}\text{Cf} \rightarrow {}^{141}\text{Cs} + {}^{111-x}\text{Tc} + xn$), for x between 0 and 6 for (a) through (g). Energy labels on the figure are given in keV with the respective PFP label.



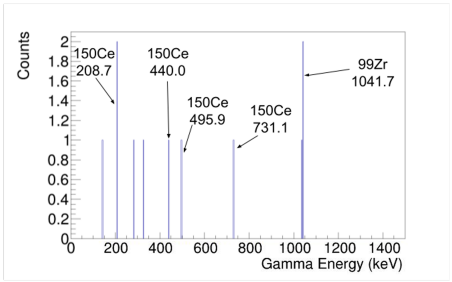
(a) 3n (b) 4n

(c) 5n (d) 6n

Figure S.6: γ energy spectra when at least two coincident γ from ^{149}Nd and at least one γ from the correlated light fragment (i.e. ^{252}Cf$\rightarrow$ ^{149}Nd+$^{103-x}$Sr+xn), for x between 3 and 6 for (a) through (d). Energy labels on the figure are given in keV with the respective PFP label.



(a) 1n (b) 2n



(c) 3n

Figure S.7: γ energy spectra when at least two coincident γ from ^{150}Ce and at least one γ from the correlated light fragment (i.e. ^{252}Cf$\rightarrow$ ^{150}Cs+$^{102-x}$Zr+xn), for x between 1 and 3 for (a) through (c). Energy labels on the figure are given in keV with the respective PFP label.

Table S.1: ^{144}Ba and light fragment compliment γ gates

Isotope	Gamma Energy Gates (keV)
^{144}Ba	196.6, 199.1, 199.326, 330.88, 559.57, 559.7, 670.8, 758.96, 785.1, 785.5
^{108}Mo	
^{107}Mo	65.4, 66.0, 99.4, 110.2, 123.4, 152.1, 165.4, 171.9, 188.9, 225.6, 233.6, 238.3, 256.1, 306.4, 326.3, 348.3, 379.5, 405.2, 405.95, 410.8, 414.5, 477.9, 478.8, 557.5, 602.8, 679.0
^{106}Mo	171.6, 350.69, 538.88, 724.5, 896.23, 1108.3
^{105}Mo	67.5, 94.8, 137.9, 139.2, 144.8, 150.0, 155.2, 159.0, 172.5, 176.0, 185.6, 210.6, 232.9, 245.8, 246.6, 246.9, 266.6, 283.0, 309.9, 314.5, 464.4, 514.0, 686.4, 775.6, 831.4
^{104}Mo	192.2, 368.4, 467.0, 609.3, 771.3
^{103}Mo	102.6, 112.7, 204.5, 564.5, 729.7, 746.3, 945.1
^{102}Mo	296.6, 401.4, 447.0

Table S.2: ^{141}Cs and light fragment compliment γ gates

Isotope	Gamma Energy Gates (keV)
^{141}Cs	47.78, 69.05, 100.721, 118.705, 369.5, 389.11, 423.89, 452.6, 459.3, 462.1, 467.81, 473.4, 481.0, 511.9, 524.5, 551.7, 556.8, 603.9, 613.06, 624.6, 626.5, 632.2, 641.19, 648.4, 687.5, 726.5, 772.9, 781.6, 802.5, 810.3, 842.7, 909.23, 1051.96
^{111}Tc	131.8, 284.2, 312.7, 375.8, 410.6, 419.5, 544.5, 552.1, 606.7, 660.2, 723.8
^{110}Tc	126.3, 178.3, 357.1, 468.1, 487.7, 616.1, 646.6, 745.8, 781.7
^{109}Tc	137.0, 298.0, 332.4, 426.2, 437.5, 440.3, 564.7, 587.6, 629.9, 633.2, 671.0, 685.5, 719.7, 761.0, 802.3
^{108}Tc	86.4, 106.2, 154.0, 218.5, 224.1, 240.5, 268.3, 312.7, 601.0, 682.7
^{107}Tc	415.4, 482.55, 509.26, 548.23, 602.28, 703.16, 733.46, 788.74
^{106}Tc	150.5, 158.4, 164.8, 254.5, 272.8, 542.5, 661.7, 717.0
^{105}Tc	187.7, 207.8, 279.14, 314.34, 364.3, 427.16, 435.7, 471.2, 495.11, 503.27, 621.20, 623.43, 625.18, 706.25, 732.24, 744.95, 784.4

Table S.3: ^{149}Nd and light fragment compliment γ gates

Isotope	Gamma Energy Gates (keV)
^{149}Nd	69.5, 108.52, 112.185, 120.395, 138.447, 162.338, 165.087, 197.194, 207.71, 227.481, 238.638, 258.327, 321.124, 322.4, 332.944, 341.31, 365.953, 389, 406.4, 430.76, 459.52, 474.57, 494.9, 517.44, 528.91, 570.72, 576.03, 642.03, 874.11
^{100}Sr	129.2, 287.8, 434.8, 566.3, 808.6, 864, 1143.4, 1186.2, 1197.4, 1201.7, 1231, 1257.1, 1285.5, 1289.5, 1328.7, 1371.3, 1392.6, 1539.4, 1827.8, 1926.8, 2115.6, 2148.4, 2211.6
^{99}Sr	90.8, 125.2, 161, 189.3, 192, 268.7, 283, 304.4, 307, 318, 422.8, 433.3, 442.9, 646.2, 683.8, 763.8, 830.8, 846.8, 854.7, 903.8, 936, 957.2, 965.1, 1003.8, 1005.5, 1064.7, 1071.6, 1104.9, 1112, 1149.8, 1211.1, 1291.8, 1578.5, 1664, 1668.6, 1972, 2230
^{98}Sr	71, 98.7, 140.6, 144.7, 207.8, 289.4, 433.3, 566.3, 630.7, 655.8, 689.5, 810.4, 1079.7, 1323.9, 1359.8, 1455.9, 1564.7, 1600.6, 1693.2, 1719.5, 1772, 1777.7, 1819.5, 1925.5, 1979.6, 2092.9, 2144.5, 2171.5
^{97}Sr	57.7, 69.1, 95.1, 141, 144.9, 167.1, 205.9, 223.8, 232.7, 237.3, 283, 355.3, 375.5, 388.4, 396, 442.9, 509.7, 520, 522.7, 522.8, 561, 575.1, 588.3, 600.5, 638, 644.6, 687.7, 735.6, 749.4, 768.7, 985.3, 1507.3

Table S.4: ^{150}Ce and light fragment compliment γ gates

Isotope	Gamma Energy Gates (keV)
^{150}Ce	97, 208.7, 232.5, 300.7, 303, 325, 376.2, 440, 495.9, 546.5, 750.1, 779.2, 890.8, 993.7, 1012.4, 1043.3, 1097.5, 1153.7, 1178, 1185.9, 1353.2
^{101}Zr	104.43, 133.67, 146.64, 152.1, 216.68, 222.6, 249.8, 259.8, 295.6, 309.98, 331.3, 378.8, 428.1, 450.2, 487.44, 510, 527.32, 562.5, 569, 575.47, 578.3, 629.1, 648.59, 670.67, 688.4, 696.7, 710.2, 712.5, 727.3, 729.57, 738.6, 746.7, 759.45, 777.6, 904, 940.2, 1119, 1297.7, 1297.89, 1300.26, 1984.7, 2023.06
^{100}Zr	118.63, 212.61, 244.8, 351.966, 616.67, 625.55, 666, 810.1, 845.2, 850.24, 1059.51, 1082.33, 1191.6, 1196.09, 1228.99, 1254.2, 1291.6, 1346.6, 1405.6, 1409.7, 1434.7, 1438.6, 1471, 1595.16, 1566.05, 1655.8, 1680
^{99}Zr	53.3, 121.7, 130.2, 143, 189.3, 192.7, 268.7, 283.3, 313.8, 392.5, 407.7, 411.6, 415, 426.7, 472.8, 476.2, 519.8, 536.2, 566, 570, 570.6, 572.3, 575.7, 600.1, 604, 614.2, 619.3, 624.2, 639.9, 706.7, 724.4, 739, 782.3, 830.8, 885.2, 929.5, 954.4, 957.2, 1003.8, 1005.5, 1041.7, 1064.7, 1074.6, 1311.1, 1548.5, 1572.7, 1834.5, 1957.4

References

Agostinelli, S., Allison, J., Amako, K., Apostolakis, J., Araujo, H., Arce, P., Asai, M., Axen, D., Banerjee, S., Barrand, G., Behner, F., Bellagamba, L., Boudreau, J., Broglia, L., Brunengo, A., Burkhardt, H., Chauvie, S., Chuma, J., Chytracek, R., Cooperman, G., Cosmo, G., Degtyarenko, P., Dell'Acqua, A., Depaola, G., Dietrich, D., Enami, R., Feliciello, A., Ferguson, C., Fesefeldt, H., Folger, G., Foppiano, F., Forti, A., Garelli, S., Giani, S., Giannitrapani, R., Gibin, D., Cadenas, J.J.G., González, I., Abril, G.G., Greeniaus, G., Greiner, W., Grichine, V., Grossheim, A., Guatelli, S., Gumplinger, P., Hamatsu, R., Hashimoto, K., Hasui, H., Heikkinen, A., Howard, A., Ivanchenko, V., Johnson, A., Jones, F.W., Kallenbach, J., Kanaya, N., Kawabata, M., Kawabata, Y., Kawaguti, M., Kelner, S., Kent, P., Kimura, A., Kodama, T., Kokoulin, R., Kossov, M., Kurashige, H., Lamanna, E., Lampén, T., Lara, V., Lefebure, V., Lei, F., Liendl, M., Lockman, W., Longo, F., Magni, S., Maire, M., Medernach, E., Minamimoto, K., Freitas, P.M.d., Morita, Y., Murakami, K., Nagamatu, M., Nartallo, R., Nieminen, P., Nishimura, T., Ohtsubo, K., Okamura, M., O'Neale, S., Oohata, Y., Paech, K., Perl, J., Pfeiffer, A., Pia, M.G., Ranjard, F., Rybin, A., Sadilov, S., Salvo, E.D., Santin, G., Sasaki, T., Savvas, N., Sawada, Y., Scherer, S., Sei, S., Sirotenko, V., Smith, D., Starkov, N., Stoecker, H., Sulkimo, J., Takahata, M., Tanaka, S., Tcherniaev, E., Tehrani, E.S., Tropeano, M., Truscott, P., Uno, H., Urban, L., Urban, P., Verderi, M., Walkden, A., Wander, W., Weber, H., Wellisch, J.P., Wenaus, T., Williams, D.C., Wright, D., Yamada, T., Yoshida, H., Zschiesche, D., . Geant4—a simulation toolkit. Nuclear Instruments and Methods in Physics Research Section A: Accelerators, Spectrometers, Detectors and Associated Equipment 506, 250–303. URL: https://www.sciencedirect.com/science/article/pii/S0168900203013688, doi:https://doi.org/10.1016/S0168-9002(03)01368-8.

National Nuclear Data Center, 2025. Information extracted from the nudat database. https://www.nndc.bnl.gov/nudat/. Accessed 2025.